AGU PUBLICATIONS

JGR

Journal of Geophysical Research: Planets

RESEARCH ARTICLE

10.1002/2017JE005426

Special Section:
Science and Exploration of the Moon, Near-Earth Asteroids, and the Moons of Mars

Formation Timescales of Amorphous Rims on Lunar Grains Derived From ARTEMIS Observations

A. R. Poppe[1,2], W. M. Farrell[2,3], and J. S. Halekas[2,4]

[1]Space Sciences Laboratory, University of California, Berkeley, CA, USA, [2]Solar System Exploration Research Virtual Institute, NASA Ames Research Center, Moffett Field, CA, USA, [3]NASA Goddard Space Flight Center, Greenbelt, MD, USA, [4]Department of Physics and Astronomy, University of Iowa, Iowa City, IA, USA

Key Points:
- We have calculated the mean ion flux to the Moon from 10 eV to 5 MeV using 5 years of ARTEMIS observations
- The mean ion spectrum at the Moon induces rim formation on lunar grains at depths up to and exceeding 500 nm
- Analysis explains the presence of anomalously thick grain rims and predicts their relationship with formation times

Supporting Information:
- Supporting Information S1
- Data Set S1

Correspondence to:
A. R. Poppe,
poppe@ssl.berkeley.edu

Citation:
Poppe, A. R., Farrell, W. M., & Halekas, J. S. (2018). Formation timescales of amorphous rims on lunar grains derived from ARTEMIS observations. *Journal of Geophysical Research: Planets*, *123*. https://doi.org/10.1002/2017JE005426

Received 17 AUG 2017
Accepted 1 DEC 2017
Accepted article online 7 DEC 2017

Abstract The weathering of airless bodies exposed to space is a fundamental process in the formation and evolution of planetary surfaces. At the Moon, space weathering induces a variety of physical, chemical, and optical changes including the formation of nanometer-sized amorphous rims on individual lunar grains. These rims are formed by vapor redeposition from micrometeoroid impacts and ion irradiation-induced amorphization of the crystalline matrix. For ion irradiation-induced rims, however, laboratory experiments of the depth and formation timescales of these rims stand in stark disagreement with observations of lunar soil grains. We use observations by the Acceleration, Reconnection, Turbulence, and Electrodynamics of the Moon's Interaction with the Sun (ARTEMIS) spacecraft in orbit around the Moon to compute the mean ion flux to the lunar surface between 10 eV and 5 MeV and convolve this flux with ion irradiation-induced vacancy production rates as a function of depth calculated using the Stopping Range of Ions in Matter model. By combining these results with laboratory measurements of the critical fluence for charged-particle amorphization in olivine, we can predict the formation timescale of amorphous rims as a function of depth in olivinic grains. This analysis resolves two outstanding issues: (1) the provenance of >100 nm amorphous rims on lunar grains and (2) the nature of the depth-age relationship for amorphous rims on lunar grains.

1. Introduction

Lunar regolith grains that are exposed to incident radiation undergo a complex series of physical, chemical, and optical changes, collectively termed "space weathering" (e.g., Hapke, 2001; Pieters et al., 2000). An understanding of space weathering is critical for the interpretation of remote observations of airless solar system bodies. Among the various forms of space weathering, laboratory analysis of returned Apollo lunar soil grains via transmission electron microscopy showed that grains often possess amorphous outer rims ranging between 20 and 250 nm thick (Bibring et al., 1972; Dran et al., 1970). Later work showed that these amorphous rims can be either similar to the host grain with some elements preferentially depleted or can be compositionally distinct from the host grain (e.g., Keller & McKay, 1993, 1994, 1997). Both types of rims are occasionally present as overlapping layers. The former rim type has generally been attributed to ion irradiation, which can preferentially sputter away certain elements present in the host grain, while the latter rim type is believed to be due to the deposition of ion-sputtered or impact-vaporized material from neighboring, geochemically distinct grains. The width of the ion-irradiated amorphous grain rims should correspond to the 20–30 nm penetration depth of ≈1 keV solar wind protons, and indeed, a majority of grain rims are consistent with this (Christoffersen et al., 1996); however, Christoffersen et al. (1996) also reported ion-irradiated grain widths of up to ≈250 nm in some grains, a finding seemingly inconsistent with 1 keV solar wind proton irradiation as a cause. Furthermore, Keller and Zhang (2015) have recently shown a correlation between the solar wind amorphized rim width and the grain exposure age calculated from solar flare track densities for lunar anorthite grains, with 20–50 nm rim widths corresponding to ages of ≈1 Myr and 150–200 nm rim widths corresponding to ≈10–50 Myr. Both the provenance of the thicker amorphous grain widths and their correlation with surface exposure time has to date remained unexplained.

With no global magnetic field or atmosphere, the lunar surface is directly exposed to fluxes of ambient charged particles. During three quarters of its orbit around the Earth, the solar wind provides the dominant flux of particles to the lunar surface consisting of ≈1 keV protons with minor contributions from alpha particles (i.e., doubly charged helium, He^{++}) (Aellig et al., 2001; Kasper et al., 2007) and multiply charged heavy ions of

solar origin (Bochsler, 1987). Passage through the Earth's magnetosheath on both the dawn and dusk flanks of the terrestrial magnetosphere exposes the Moon to shocked (i.e., subsonic and highly thermalized) solar wind plasma for approximately 2–4 days per lunation. Deeper within the magnetotail, particle fluxes are typically several orders-of-magnitude lower at the Moon during monthly transits, although geomagnetic activity can stimulate significant fluxes of particles in the lunar vicinity in both the earthward and tailward directions, potentially consisting of both solar wind (i.e., H^+ and He^{++}) and terrestrial species (i.e., H^+, He^+, O^+, N_2^+, NO^+, and O_2^+) (e.g., Christon et al., 1994; Kistler et al., 2010; Lui et al., 1998; Poppe et al., 2016; Seki et al., 1998). Finally, the Moon is also intermittently exposed to fluxes of ≈1–100 keV protons in the terrestrial ion foreshock region (e.g., Eastwood et al., 2005; Gosling et al., 1982, 1989; Lin et al., 1974), the various implications of which have only recently been explored (Nishino et al., 2017) and solar energetic particle events with energies ranging from keV to GeV scales (e.g., Reames, 1999, 2013; Schwadron et al., 2012).

Here we use a combination of 5 years of observations by the Acceleration, Reconnection, Turbulence, and Electrodynamics of the Moon's Interaction with the Sun (ARTEMIS) mission (Angelopoulos, 2011), simulations with the Stopping Range of Ions in Matter (SRIM) (Ziegler et al., 1985, 2008, 2010) model, and laboratory measurements of the critical charged-particle irradiation amorphization fluence in olivine (Carrez et al., 2002) to quantify the depth and associated timescales of charged-particle weathering on olivinic lunar grains. This work builds upon and extends previous analyses of solar wind-irradiation produced amorphous rims on lunar and asteroidal grains (Chamberlin et al., 2008; Christoffersen & Keller, 2015) and qualitatively relates to the rim thickness-age relationship reported for lunar anorthite grains (Keller & Zhang, 2015). We show that the average ion spectrum incident upon the lunar surface between 10 eV and 5 MeV explains the presence of lunar grains with rims >100 nm and predicts the relationship between amorphous rim thickness and exposure age. These findings have fundamental implications for understanding the microphysical and optical properties of lunar regolith and airless silicate bodies throughout the solar system, including, for example, laboratory studies of regolith grains returned from asteroid (25143) Itokawa by the Hayabusa spacecraft (e.g., Matsumoto et al., 2015; Noguchi et al., 2014) and the anticipated return of regolith samples from asteroid (101955) Bennu by NASA's OSIRIS-REx mission (Lauretta et al., 2015).

2. ARTEMIS Observations

The ARTEMIS mission consists of a pair of identically instrumented spacecraft in orbit around the Moon since mid-2011 (Angelopoulos, 2011; Sibeck et al., 2011). The two ARTEMIS probes are in highly elliptical orbits near the lunar equatorial plane with periselenes varying between 10 and 500 km altitude and aposelenes between 10 and 12 lunar radii (1 R_L = 1,738 km). Both probes measure the in situ magnetic field vector (Auster et al., 2008) and low (1–25,000 eV) and high (30 keV–5 MeV) energy ion and electron distributions with the electrostatic analyzer (ESA) (McFadden et al., 2008) and Solid State Telescope (SST) instruments, respectively. The magnetic field is sampled at a minimum frequency of 4 Hz, and the three-dimensional particle distributions are measured every ≈0.25 Hz. We first analyze two examples of ARTEMIS observations that illustrate periods in which the near-lunar environment contained ions with energies exceeding the typical ≈1 keV of solar wind protons.

Figure 1 shows 6 h of ARTEMIS observations while the Moon was in the solar wind on 6 January 2013 including (a) lunar position in Geocentric-Solar-Ecliptic (GSE) coordinates, (b) ARTEMIS P1 and P2 probe orbits in Selenocentric-Solar-Ecliptic (SSE) coordinates, (c) interplanetary magnetic field (IMF) vector, (d and e) ion energy spectra for P1 and P2, respectively, and (f and g) ion angular spectra for P1 and P2, respectively. As shown in Figure 1a, the IMF (gray lines) was oriented such that the Moon was magnetically connected to the quasi-parallel terrestrial bow shock (solid black line), placing the Moon and ARTEMIS probes squarely in the ion foreshock region (e.g., Gosling et al., 1982, 1989; Lin et al., 1974). Ion fluxes during this period consist of both the solar wind near 600 eV (equivalent to a bulk velocity of 340 km/s) along with intermittent bursts of 1–20 keV foreshock ion flux (e.g., see also Nishino et al., 2017). Foreshock ions originate as inflowing solar wind protons that are scattered and accelerated away from the Earth's bow shock by processes such as pitch angle scattering from low-frequency plasma waves at the shock foot and diffusive particle acceleration from wave-particle interactions within the foreshock region (e.g., Balogh & Treumann, 2013, chapter 6).

Figure 2 shows 2 days of ARTEMIS observations taken in the terrestrial magnetotail on 2–4 February 2015 including (a) the lunar position in Geocentric-Solar-Ecliptic (GSE) coordinates, (b) ARTEMIS P1 and P2 probe orbits in Selenocentric-Solar-Ecliptic (SSE) coordinates, (c) the magnetic field vector, (d and e) the ARTEMIS P1

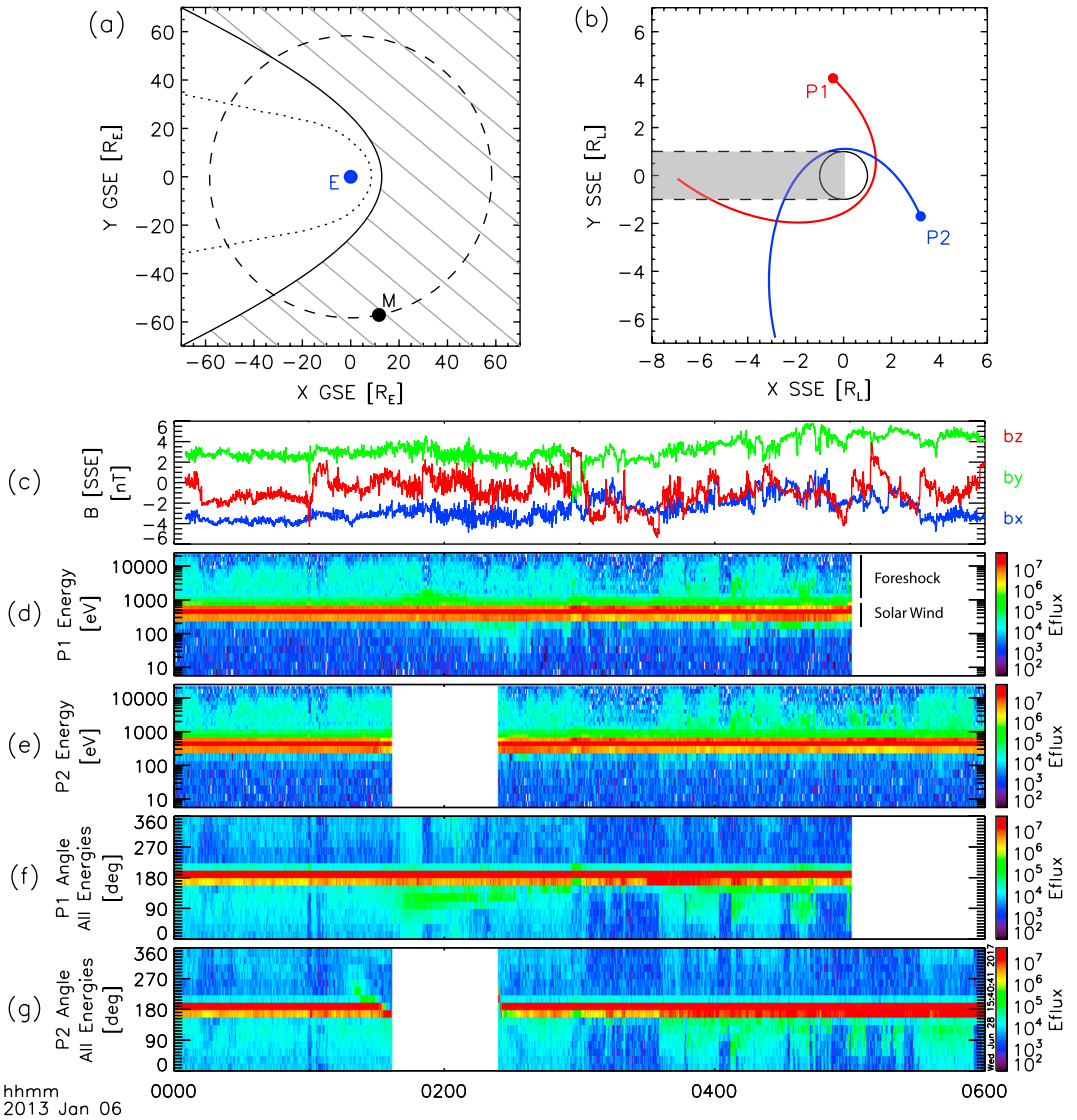

Figure 1. ARTEMIS observations of ion flux in the terrestrial foreshock on 6 January 2013. (a) The lunar position, "M," in GSE coordinates, the Earth's position, "E," the lunar orbit (dashed line), terrestrial bow shock (solid black line), magnetopause (dotted line), and interplanetary magnetic field configuration for this time period (gray solid lines). (b) The ARTEMIS P1 and P2 orbits in SSE coordinates, with the lunar optical shadow denoted in gray. The (c) interplanetary magnetic field, (d) P1 ESA ion energy flux, (e) P2 ESA ion energy flux, (f) P1 ion angular flux, and (g) P2 ion angular flux. Periods of time during which the respective probes are in the lunar wake region are left blank in Figures 1d–1g.

low (ESA) and high (SST) energy ion spectra, and (f and g) the ARTEMIS P2 low (ESA) and high (SST) energy ion spectra. During this period, ion fluxes from the terrestrial current sheet are present at energies ranging from 50 eV to 500 keV. The high current sheet energies at the lunar orbit during this time are correlated with above-average solar wind speeds of 600–700 km/s as observed upstream of the Earth by the Wind spacecraft (not shown). Such a correlation between upstream solar wind energy and terrestrial current sheet temperatures near-lunar orbit has recently been shown using the full 5 year ARTEMIS data set (Artemyev et al., 2017), demonstrating that upstream heliospheric plasma conditions can influence the lunar plasma environment, even while the Moon is "protected" within the magnetotail.

Taking these two examples as motivation, we calculated the mean ion energy flux in near-lunar space by averaging 5 years (January 2012 to December 2016) of ARTEMIS P1 and P2 ESA and SST observations. First, for each probe individually, we excluded periods when (1) the probe was at selenographic altitudes less than

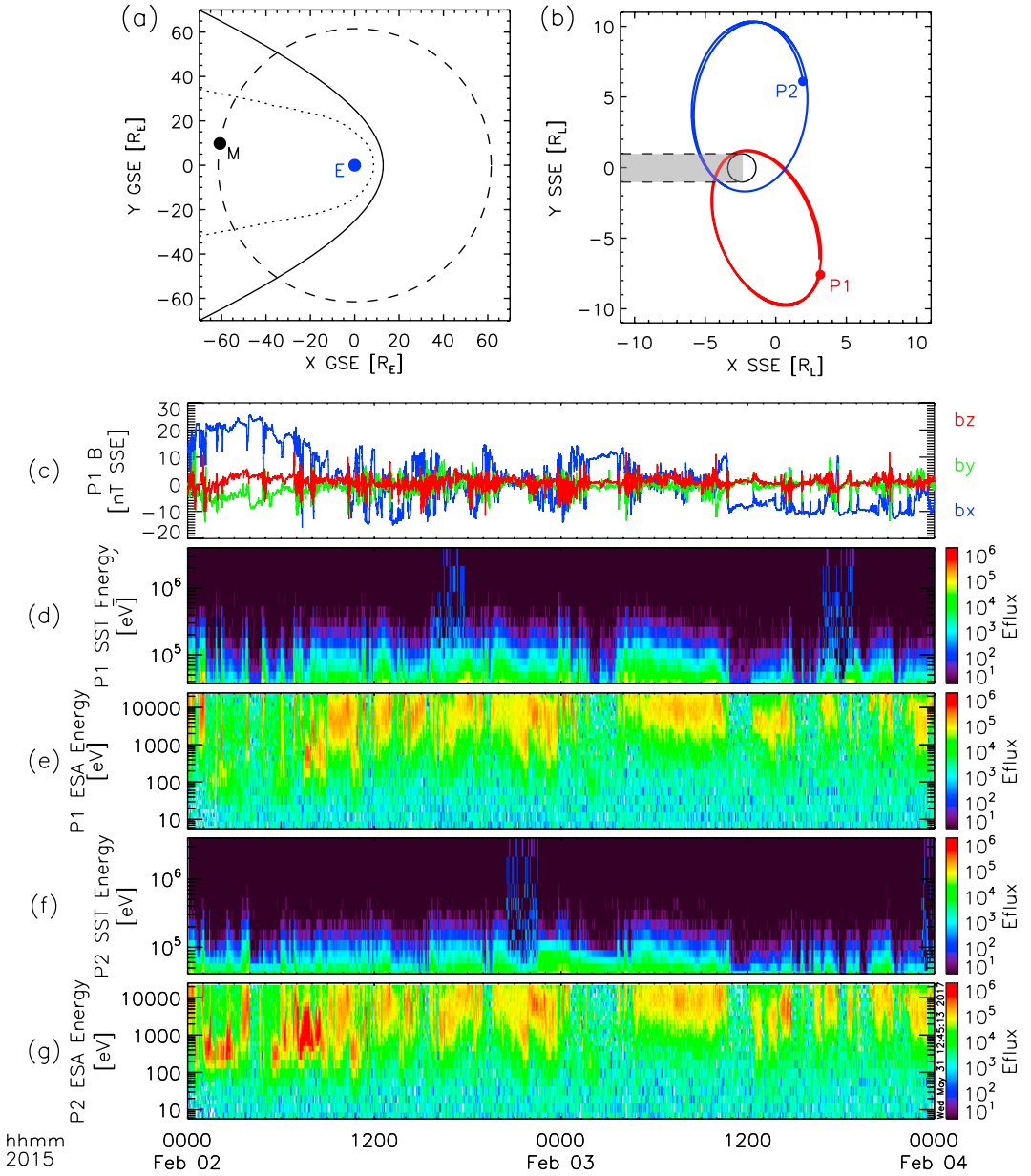

Figure 2. ARTEMIS observations of ion flux in the terrestrial magnetotail on 2–4 February 2014. (a) The lunar position in GSE coordinates and (b) the ARTEMIS probe orbits in SSE coordinates in the same manner as Figures 1a and 1b. The (c) magnetic field, (d) P1 SST ion energy flux, (e) P1 ESA ion energy flux, (f) P2 SST ion energy flux, and (g) P2 ESA ion energy flux.

1 lunar radius, (2) the probe was near or within the lunar wake defined as a cylindrical volume of space 1.5 lunar radii in radius extending antisunward from the Moon, and (3) for SST specifically, we excluded all data when the probe was sunward of the Moon. Filters (1) and (2) prevent inclusion of ion flux spectra that have been disturbed by electrodynamic interactions with the Moon (e.g., Futaana et al., 2003; Halekas et al., 2013; Lue et al., 2011; Poppe et al., 2017), and filter (3) removes periods when the SST detectors experience contamination from sunlight reflected from the lunar surface (i.e., moonshine). Second, we performed a background subtraction to both the ESA and SST count rates. To do so, we identified 11 days during which the ARTEMIS probes were exposed to the quiescent solar wind and observed no sign of energetic particle activity. For ESA, we used all observations at the lowest five energy bins (≈5–20 eV, therefore much below the solar wind energy) to compute a mean background count rate per observation at an individual energy/angle bin. For SST, we used these quiet-time observations to determine the mean background count rate per observation for each

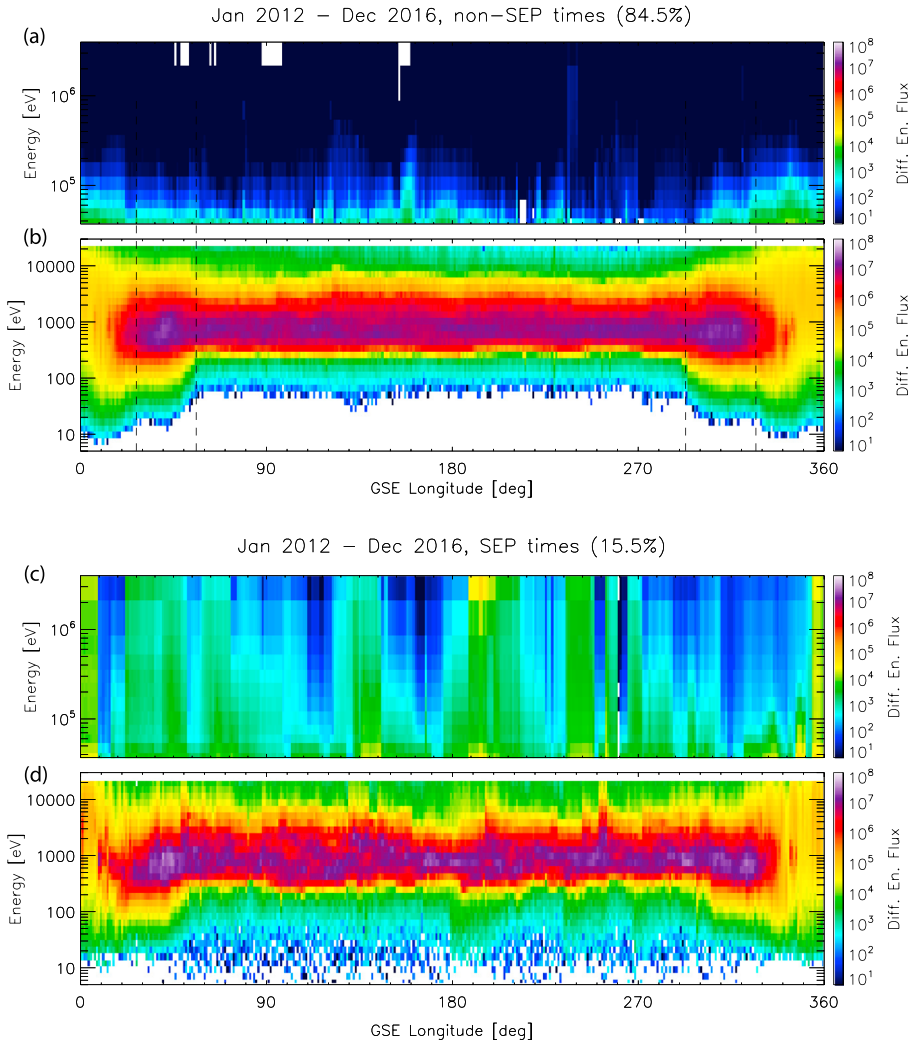

Figure 3. The mean differential ion energy flux as a function of energy and lunar GSE longitude (i.e., lunar phase) for (a and b) non-SEP times and (c and d) SEP times. The dashed lines in Figures 3a and 3b denote observed plasma boundaries (bow shock and magnetopause) as described in the text.

energy bin individually. These backgrounds were then subtracted from the ARTEMIS ESA and SST count rates before conversion to differential flux.

After the background subtraction, we separated the data set into periods with solar energetic particle (SEP) events and those without. SEP times comprised approximately 15% of the data set and times without SEP events comprised 85%. For each of these subsets, we then computed the average differential ion energy flux as a function of GSE longitude (i.e., lunar phase) in 1° bins. Figure 3 shows the average flux for (a and b) non-SEP and (c and d) SEP events, respectively, as a function of GSE longitude (note that longitude 0/360° is "full moon" and 180° is "new moon," for reference). For the non-SEP events, we easily identified distinct plasma boundaries between the solar wind/foreshock and magnetosheath (i.e., the terrestrial bow shock), and between the terrestrial magnetosheath and the terrestrial magnetotail (i.e., roughly the magnetopause). The vertical dashed lines in Figures 3a and 3b denote these plasma environment boundaries. For the non-SEP times, these three plasma environments were averaged separately in order to isolate their respective contributions to the mean flux. For the SEP times, the plasma boundaries are somewhat observable; however, we nonetheless averaged the SEP event spectrum across all GSE longitudes. We also note that as the ARTEMIS ESA and SST instruments cannot distinguish ion mass, we must therefore estimate the contribution of alpha particles (i.e., doubly charged helium) to the mean ion flux. In situ observations by the IMP 6, 7, and 8 spacecraft (e.g., Borrini et al., 1981, 1982, 1983), the Wind/SWE instrument (Aellig et al., 2001; Kasper et al., 2007), and

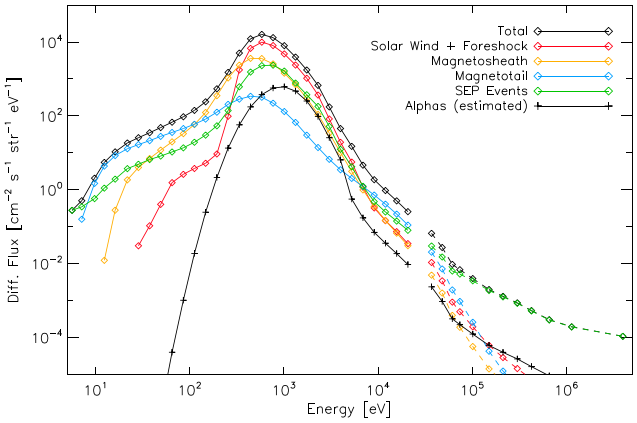

Figure 4. The mean ion spectrum at the Moon as calculated from the ARTEMIS observations (black diamonds). Colored curves denote the contributions to the mean flux from the solar wind/terrestrial foreshock (red), magnetosheath (orange), magnetotail (blue), and solar energetic particle (SEP) events (green). The fraction of the observed flux due to alpha (He^{++}) particles is estimated as shown by the black crosses. The gap near 30 keV is due to the transition of the ESA instrument (1–25,000 eV) to the SST instrument (30 keV–3 MeV). These data are provided in readable format in the supporting information.

the Genesis solar wind collection plates (Reisenfeld et al., 2013) have measured the mean values and variability in the alpha fraction in the solar wind as a function of solar wind regime. Analysis of Wind/SWE measurements found a 250 day average helium fraction between 1% and 5%, along with correlations with solar wind speed, heliographic latitude, and solar cycle (Kasper et al., 2007). Solar wind alpha content observed by Genesis also varied by solar wind regime, including solar wind, fast wind, and coronal mass ejection time periods (Reisenfeld et al., 2013); nevertheless, mean alpha fractions observed by Genesis ranged from 3 to 5%. Thus, for the core solar wind alpha population, we used the solar wind velocity distribution from Dmitriev et al. (2011) to derive an alpha distribution with 4% the flux of the solar wind (see also Bochsler, 1987, Table 1). In addition to the core solar wind alpha distribution, we added 3% of the solar energetic particle flux as alphas at energies above 1 keV (Kahler et al., 2009).

Figure 4 shows the average differential ion flux (black curve), which peaks at values of 10^4 cm^{-2} s^{-1} str^{-1} eV^{-1} near 600 eV dominated by the solar wind (red curve) with additional contributions from the magnetosheath (orange), magnetotail (blue), and SEP events (green). Between approximately 5 and 50 keV, the average flux decreases yet is composed of nearly equal contributions from all four ambient plasma environments. At energies of 50 keV and above, SEP events are dominant, with only minor contributions from the solar wind/foreshock, magnetosheath, and magnetotail. The estimated flux of alpha particles has a peak near 1.5 keV with an extended tail at higher energies resulting mainly from SEP events. Thus, contrary to the first-order picture of the Moon exposed to a 1 keV solar wind proton beam with monthly transits through an extremely low flux magnetotail, Figure 4 demonstrates that the combination of terrestrial ion foreshock flux (e.g., Eastwood et al., 2005), terrestrial magnetosheath and magnetotail current sheet flux, and solar energetic particle events (Gopalswamy et al., 2004; Reames, 2013; Schwadron et al., 2012) provides ion fluxes to the Moon at energies much greater than typically expected from the solar wind alone.

3. Amorphous Rim Thicknesses and Formation Timescales

To quantify the thickness of amorphous rims on lunar soil induced by the mean ion flux spectrum at the Moon, we used the Stopping Range of Ions in Matter (SRIM) Monte Carlo program (Ziegler et al., 1985, 2008, 2010) to calculate the damage produced in lunar soil grains as a function of incident ion energy, species, and depth. As discussed in previous reports (e.g., Chamberlin et al., 2008; Christoffersen & Keller, 2011, 2015; Gray & Edmunds, 2004; May et al., 2000; Ziegler et al., 1985, 2008), the SRIM model numerically calculates the interactions of energetic ions with target surface materials through electronic (i.e., ionization) and nuclear (i.e., elastic collisions) interactions. SRIM requires specification of both the projectile ion data including species, incident energy, and incident angle and the target material properties, including composition, density, layer thickness, and parameters of the target crystal lattice. The lattermost of these requirements includes the surface energy, displacement energy, and lattice binding energies of the target crystal and is discussed in further detail in May et al. (2000) and Gray and Edmunds (2004); however, as noted at length in Christoffersen and Keller (2011), an a priori calculation of these values for a given mineral is not possible. Thus, for consistent comparison, values used in previous investigations are typically used. An additional, important limitation of the SRIM model is the assumption of an unmodified target throughout; in other words, the model does not account for the alteration of the target via sputtering, displacements, amorphization, etc., over time. Finally, SRIM simulation results of displacements-per-atom as a function of depth and incident ion parameters can only be translated into quantitative amorphization timescales via the use of experimentally determined critical amorphization ion fluences for a given mineral (e.g., Carrez et al., 2002). Despite these SRIM shortcomings, we nevertheless find it instructive to connect the observed ARTEMIS solar wind energy distribution to SRIM model-derived crystal modification to get an estimate of the crystal damage at depth. We can then compare this estimate to other published profiles of weathering and rim formation rates.

For our analysis, we injected 10^5 protons and alphas, respectively, at the center energy of each ARTEMIS ESA and SST energy bin into an olivine surface at 45° incidence angle. We used an Fo50 olivine composition ($MgFeSiO_4$) with a density of 3.8 kg m^{-3}. The surface, displacement, and lattice binding energies for olivine

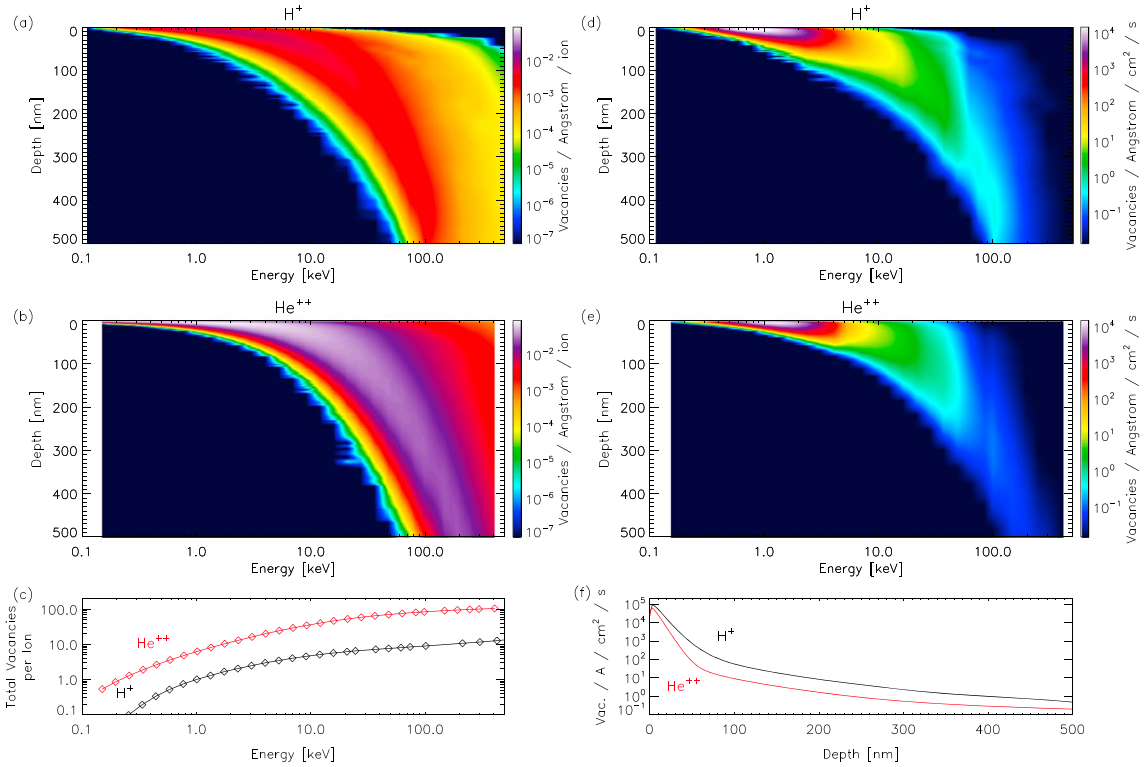

Figure 5. (a and b) SRIM simulation results of the vacancy production as a function of ion energy and depth for protons and alphas, respectively. (c) The total number of vacancies per ion as a function of energy for protons (black) and alphas (red). (d and e) The vacancy production rates as a function of energy and depth for protons and alphas, respectively. (f) The vacancy production rate integrated over all ion energies as a function of depth for protons and alphas.

were taken from Gray and Edmunds (2004, Table 1), who used an earlier version of SRIM to model ion irradiation of olivinic grains. For each incident ion energy, SRIM tabulates the number of vacancies (i.e., the number of times an incident ion dislodged a crystalline atom) as a function of depth in the material, which is then normalized to number of vacancies per incident ion. For all simulations for both protons and alphas, we used a target thickness greater than the maximum penetration depth for each individual energy, ensuring that all collisions and vacancies are captured. Figures 5a and 5b show the distribution of vacancies produced per interval depth per incident proton and alpha, respectively, as a function of energy and depth. Vacancy production is a strong function of ion energy. Protons less than 1 keV produce vacancies at depths of ≈10–20 nm, consistent with previous analyses (e.g., Christoffersen et al., 1996). As the proton energy increases above 1 keV, vacancies are produced to greater depths and over broader regions, with 10 keV protons producing peak vacancies near 40 nm depth and 100 keV protons producing peak vacancies at depths near 500 nm. As shown in Figure 5b, alphas produce vacancies at peak depths over the relevant solar wind energy range (0.5–10 keV) mainly between 10 and 50 nm, with vacancy production depth increasing with incident energy similar to protons. Figure 5c shows the total number of vacancies per incident ion, calculated by integrating the distributions shown in Figures 5a and 5b over depth. At an equal energy, an alpha particle produces approximately 10 times the number of vacancies as a proton.

We calculated the vacancy production rates in lunar soil by convolving the SRIM simulation results in Figures 5a and 5b with the mean differential ion flux at the Moon observed by ARTEMIS for protons (summed over plasma environments) and estimated for alphas, as shown in Figure 4. Figures 5d and 5e show the production rate of vacancies in lunar grains for protons and alphas, respectively. The peak production rate of vacancies by protons occurs at energies of 500 eV to 2 keV at depths of 10–20 nm, consistent with earlier results (e.g., Christoffersen et al., 1996); however, proton fluxes at energies higher than the typical solar wind induce vacancies at depths up to 500 nm albeit at decreasing rates. Alphas, Figure 5e, show qualitatively similar vacancy production behavior to protons with peak production occurring at a depth of 10–20 nm near alpha energies of approximately 1.5 keV and an extended, slower production of vacancies at depths up to and beyond 500 nm. Finally, Figure 5f shows the vacancy production rates as a function of depth for protons

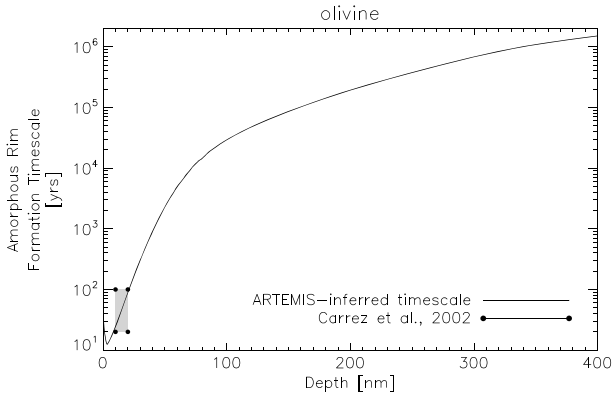

Figure 6. The weathering timescale as a function of depth as determined from the convolution of the ARTEMIS mean ion flux, the SRIM vacancy production rates, and the inferred timescale for 10–20 nm olivinic rim formation from Carrez et al. (2002). The minimum in the timescale near 5 nm as opposed to at the surface is due to the peak in ion flux near 0.5 keV (i.e., Figure 4) that causes a corresponding peak in the vacancy production rate near 5 nm.

and alphas integrated over all incident energies. Both protons and alphas contribute to vacancy production extending to depths of 500 nm and greater, with protons generating approximately a factor of 5 greater number of vacancies than alphas at all depths. We conclude from this that >100 nm grain rims are caused by energetic (i.e., > ~10 keV) protons and alphas incident upon the lunar surface at higher fluxes than previously appreciated.

Finally, the vacancy production rates shown in Figure 5f can be inverted to establish the weathering timescale of exposed lunar soil for grain compositions for which the amorphization fluence has been experimentally measured. Carrez et al. (2002) have measured a critical charged-particle amorphization fluence of between 1 and 5×10^{16} He^{+} ions/cm^2/s for ultrathin olivine sections exposed to 4 keV He^{+} ions (i.e., typical solar wind alpha energies). Along with the concurrent flux of protons expected in the solar wind, this fluence is achieved at the Moon between 20 and 100 years. Taking this timescale as representative of the formation time of a 10–20 nm thick rim (i.e., a thickness equivalent to that generated by only 1 keV solar wind protons and 4 keV solar wind alphas), we can "calibrate" the ARTEMIS+SRIM-derived relative timescales. Figure 6 shows the charged-particle weathering timescale determined via this method compared to the inferred rim width-age data of Carrez et al. (2002), predicting that, for example, 100 nm thick amorphous rims should develop in olivine grains in approximately 50,000 years and 400 nm amorphous rims should develop in just under 3 Myr. Formation times for rims with thicknesses less than ≈100 nm qualitatively agree with those presented in Christoffersen and Keller (2015) while the buildup of >100 nm rims extends to periods beyond those considered in Christoffersen and Keller (2015). We also suggest that the shape of the amorphous formation timescale for olivine presented here may also, at least qualitatively, explain the rim width-age relationship seen in anorthite grains as reported by Keller and Zhang (2015), despite the lack of an experimentally measured critical amorphization fluence for anorthite.

4. Conclusion

The analysis of ARTEMIS mean ion flux to the Moon has resolved two outstanding questions with regards to the nature of space weathering and regolith grain modification at the Moon, namely, the formation of >100 nm grain rims and the correlation of rim widths with solar wind exposure timescales. In addition to the core solar wind beam near 1 keV, high-energy ion fluxes originate from the Earth's terrestrial foreshock (e.g., Eastwood et al., 2005; Gosling et al., 1982, 1989; Lin et al., 1974), the high-temperature terrestrial magnetosheath and magnetotail current sheet (e.g., Artemyev et al., 2017), and solar energetic particle events (e.g., Gopalswamy et al., 2004; Reames, 2013). The ion flux peaks at solar wind energies corresponding to the rapid formation of 10–20 nm rims on lunar grains, while energies above 1 keV decrease in flux relative to the solar wind and thus induce thicker rim formation on longer timescales. In a broader sense, the results shown here emphasize that the plasma environment at the Moon is richer than the first-order assumption of 1 keV solar wind proton/4 keV solar wind alpha flux to the Moon.

While our analysis here has focused on the mean ambient plasma environment at the Moon and its role in weathering lunar grains, the results also have implications for airless body surface weathering throughout the solar system. For example, the mean ion flux spectrum for the solar wind and SEP events shown in Figure 4 can also explain the presence of anomalously thick grain rims observed on samples returned from asteroid (25143) Itokawa by the Hayabusa mission (Matsumoto et al., 2015; Noguchi et al., 2014). Indeed, Matsumoto et al. (2015) reported an amorphous rim width on an Itokawa grain of 125–145 nm and attributed this to an inferred flux of 10 keV He^{++} ions from the solar wind. As shown here, however, such a rim is rather most likely formed by the flux of both protons and alphas present in solar energetic particle events, as opposed to solely from the high speed tail of the solar wind alpha distribution. The near-Earth asteroid (101955) Bennu, to be visited by NASA's OSIRIS-REx mission in 2018, will return a sample of regolith surface material and will allow for further analysis of the nature of space weathered rims on airless rocky bodies (Lauretta et al., 2015). Finally, Mars' two moons Phobos and Deimos also represent an important case to study in this regard, despite the current lack of surface samples. The ambient plasma environment at these two moons consists of exposure to both the solar wind and the Martian magnetosphere, the latter of which is rich in heavy, planetary ions

such as O^+, O_2^+, and CO_2^+ (e.g., Brain et al., 2015; Curry et al., 2014; Dong et al., 2015; Poppe & Curry, 2014; Rahmati et al., 2015). The fluxes of these heavy planetary ions should alter the weathered rim depth-timescale relationship, and future predictive studies using the in situ Mars Atmosphere and Volatile Evolution plasma data set (e.g., Halekas et al., 2015; Jakosky et al., 2014; McFadden et al., 2015) are a potentially promising line of inquiry leading up to eventual Phobos and/or Deimos surface sample return missions (e.g., Murchie et al., 2014).

Acknowledgments
The authors gratefully acknowledge support from NASA's Solar System Exploration Research Virtual Institute, grants NNX14AG16A and NNX15AH15A. A. R. P. also thanks D. L. Turner for assistance with processing SST data. The ARTEMIS mission is funded and operated under NASA grant NAS5-02099, and we specifically acknowledge J. P. McFadden for the use of ESA data, D. E. Larson for the use of SST data, and K. -H. Glassmeier, U. Auster, and W. Baumjohann for the use of FGM data provided under the lead of the Technical University of Braunschweig and with financial support through the German Ministry for Economy and Technology and the German Center for Aviation and Space (DLR), contract 50 OC 0302. All ARTEMIS data necessary to reproduce this work are publicly available at http://artemis.ssl.berkeley.edu, and the SRIM simulation software can be downloaded freely from http://www.srim.org. The authors thank R. Christoffersen and an anonymous reviewer for constructive reviews.

References

Aellig, M. R., Lazarus, A. J., & Steinberg, J. T. (2001). The solar wind helium abundance: Variation with wind speed and the solar cycle. *Geophysical Research Letters*, *28*(14), 2767–2770. https://doi.org/10.1029/2000GL012771

Angelopoulos, V. (2011). The ARTEMIS mission. *Space Science Reviews*, *165*, 3–25.

Artemyev, A. V., Angelopoulos, V., Hietala, H., Runov, A., & Shinohara, I. (2017). Ion density and temperature profiles along (X_{GSM}) and across (Z_{GSM}) the magnetotail as observed by THEMIS, Geotail, and ARTEMIS. *Journal of Geophysical Research: Space Physics*, *122*, 1590–1599. https://doi.org/10.1002/2016JA023710

Auster, H. U., Glassmeier, K. H., Magnes, W., Aydogar, O., Baumjohann, W., & Constantinescu, D. (2008). The THEMIS fluxgate magnetometer. *Space Science Reviews*, *141*(1–4), 235–264.

Balogh, A., & Treumann, R. A. (2013). Physics of collisionless shocks (ISSI Scientific Report 12). New York: Springer.

Bibring, J. P., Duraud, J. P., Durrieu, L., Jouret, C., Maurette, M., & Meunier, R. (1972). Ultrathin amorphous coatings on lunar dust grains. *Science*, *175*, 753–755.

Bochsler, P. (1987). Solar wind ion composition. *Physica Scripta*, *T18*, 55–60.

Borrini, G., Gosling, J. T., Bame, S. J., Feldman, W. C., & Wilcox, J. M. (1981). Solar wind helium and hydrogen structure near the heliospheric current sheet: A signal of coronal streamers at 1 AU. *Journal of Geophysical Research*, *86*(A6), 4565–4573.

Borrini, G., Gosling, J. T., Bame, S. J., & Feldman, W. C. (1982). Helium abundance enhancements in the solar wind. *Journal of Geophysical Research*, *87*(A9), 7370–7378.

Borrini, G., Gosling, J. T., Bame, S. J., & Feldman, W. C. (1983). Helium abundance variations in the solar wind. *Solar Physics*, *83*, 367–378.

Brain, D. A., McFadden, J. P., Halekas, J. S., Connerney, J. E. P., Bougher, S. W., Curry, S., … Seki, K. (2015). The spatial distribution of planetary ion fluxes near Mars observed by MAVEN. *Geophysical Research Letters*, *42*, 9142–9148. https://doi.org/10.1002/2015GL065293

Carrez, P., Demyk, K., Cordier, P., Gengembre, L., Grimblot, J., D'Hendecourt, L., … Leroux, H. (2002). Low-energy helium ion irradiation-induced amorphization and chemical changes in olivine: Insights for silicate dust evolution in the interstellar medium. *Meteoritics and Planetary Science*, *37*, 1599–1614.

Chamberlin, S., Christoffersen, R., & Keller, L. (2008). Space plasma ion processing of the lunar soil: Modeling of radiation-damaged rim widths on lunar grains. In *Proceedings of the 39th Lunar and Planetary Science Conference* (2302 pp.). Houston, TX: Lunar and Planetary Institute.

Christoffersen, R., & Keller, L. P. (2011). Space radiation processing of sulfides and silicates in primitive solar systems material: Comparative insights from in situ TEM ion irradiation experiments. *Meteoritics and Planetary Science*, *46*(7), 950–969.

Christoffersen, R., & Keller, L. P. (2015). Solar ion processing of Itokawa grains: Constraints on surface exposure times. In *Proceedings of the 46th Lunar and Planetary Science Conference* (2084 pp.). Houston, TX: Lunar and Planetary Institute.

Christoffersen, R., Keller, L. P., & McKay, D. S. (1996). Microstructure, chemistry, and origin of grain rims on ilmenite from the lunar soil finest fraction. *Meteoritics and Planetary Science*, *31*, 835–848.

Christon, S. P., Gloeckler, G., Williams, D. J., Mukai, T., McEntire, R. W., Jacquey, C., … Yamamoto, T. (1994). Energetic atomic and molecular ions of ionospheric origin observed in distant magnetotail flow-reversal events. *Geophysical Research Letters*, *21*(25), 3023–3026.

Curry, S. M., Liemohn, M., Fang, X., Ma, Y., Slavin, J., Espley, J., … Dong, C. F. (2014). Test particle comparison of heavy atomic and molecular ion distributions at Mars. *Journal of Geophysical Research: Space Physics*, *119*, 2328–2344. https://doi.org/10.1002/2013JA019221

Dmitriev, A. V., Suvorova, A. V., & Veselovsky, I. S. (2011). Statistical characteristics of the heliospheric plasma and magnetic field at Earth's orbit during four solar cycles 20-23. In H. E. Johannson (Ed.), *Handbook on solar wind: Effects, dynamics, and interactions* (chap. 2, pp. 81–144). New York: NOVA Science Publishers.

Dong, Y., Fang, X., Brain, D. A., McFadden, J. P., Halekas, J. S., Connerney, J. E., … Jakosky, B. M. (2015). Strong plume fluxes at Mars observed by MAVEN: An important planetary ion escape channel. *Geophysical Research Letters*, *42*, 8942–8950. https://doi.org/10.1002/2015GL065346

Dran, J. C., Durrieu, L., Jouret, C., & Maurette, M. (1970). Habit and texture studies of lunar and meteoritic materials with a 1 MeV electron microscope. *Earth and Planetary Science Letters*, *9*, 391–400.

Eastwood, J. P., Lucek, E. A., Mazelle, C., Meziane, K., Narita, Y., Pickett, J., & Treumann, R. A. (2005). The foreshock. *Space Science Reviews*, *118*, 41–94.

Futaana, Y., Machida, S., Saito, Y., Matsuoka, A., & Hayakama, H. (2003). Moon-related nonthermal ions observed by Nozomi: Species, sources, and generation mechanisms. *Journal of Geophysical Research*, *108*(A1), 1025. https://doi.org/10.1029/2002JA009366

Gopalswamy, N., Yashiro, S., Krucker, S., Stenborg, G., & Howard, R. A. (2004). Intensity variation of large solar energetic particle events associated with coronal mass ejections. *Journal of Geophysical Research*, *109*, A12105. https://doi.org/10.1029/2004JA010602

Gosling, J. T., Thomsen, M. F., Bame, S. J., Feldman, W. C., Paschmann, G., & Sckopke, N. (1982). Evidence for specularly reflected ions upstream from the quasi-parallel bow shock. *Geophysical Research Letters*, *9*(12), 1333–1336.

Gosling, J. T., Thomsen, M. F., Bame, S. J., & Russell, C. T. (1989). On the source of diffuse, suprathermal ions observed in the vicinity of the Earth's bow shock. *Journal of Geophysical Research*, *94*(A4), 3555–3563.

Gray, M. D., & Edmunds, M. G. (2004). Modification of dust-grain structure by sputtering. *Monthly Notices of the Royal Astronomical Society*, *349*, 491–502.

Halekas, J. S., Poppe, A. R., McFadden, J. P., & Glassmeier, K.-H. (2013). The effects of reflected protons on the plasma environment of the Moon for parallel interplanetary magnetic fields. *Geophysical Research Letters*, *40*, 4544–4548. https://doi.org/10.1002/grl.50892

Halekas, J. S., Taylor, E. R., Dalton, G., Johnson, G., Curtis, D. W., McFadden, J. P., … Jakosky, B. M. (2015). The solar wind ion analyzer for MAVEN. *Space Science Reviews*, *195*(1–4), 125–151.

Hapke, B. (2001). Space weathering from Mercury to the asteroid belt. *Journal of Geophysical Research*, *106*(E5), 10,039–10,073. https://doi.org/10.1029/2000JE001338

Jakosky, B. M., Lin, R. P., Grebowsky, J. M., Luhmann, J. G., Mitchell, D. F., Beutelschies, G., … Zurek, R. (2014). The 2013 Mars Atmosphere and Volatile Evolution (MAVEN) mission to Mars. *Space Science Reviews*, *195*(1–4), 3–48.

Kahler, S. W., Tylka, A. J., & Reames, D. V. (2009). A comparison of elemental abundance ratios in SEP events in fast and slow solar wind regions. *Astrophysical Journal*, *701*, 561–570.

Kasper, J. C., Stevens, M. L., Lazarus, A. J., Steinberg, J. T., & Ogilvie, K. W. (2007). Solar wind helium abundance as a function of speed and heliographic latitude: Variation through a solar cycle. *Astrophysical Journal*, *660*, 901–910.

Keller, L. P., & McKay, D. S. (1993). Discovery of vapor deposits in the lunar regolith. *Science*, *261*, 1305–1307.

Keller, L. P., & McKay, D. S. (1994). The contribution of vapor deposition to amorphous rims on lunar soil grains. *Meteoritics*, *29*, 480.

Keller, L. P., & McKay, D. S. (1997). The nature and origin of rims on lunar soil grains. *Geochimica et Cosmochimica Acta*, *61*(11), 2331–2341.

Keller, L. P., & Zhang, S. (2015). Rates of space weathering in lunar soils. In *Space weathering of airless bodies: An integration of remote sensing data, laboratory experiments and sample analysis workshop* (2056 pp.). Houston, TX: LPI Contribution No. 1878.

Kistler, L. M., Galvin, A. B., Popecki, M. A., Simuna, K. D. C., Farrugia, C., Möbius, E., … Russell, C. T. (2010). Escape of O^+ through the distant tail plasma sheet. *Geophysical Research Letters*, *37*, L21101. https://doi.org/10.1029/2010GL045075

Lauretta, D. S., Bartels, A. E., Barucci, M. A., Bierhaus, E. B., Binzel, R. P., Bottke, W. F., … Walsh, K. J. (2015). The OSIRIS-REx target asteroid (101955) Bennu: Constraints on its physical, geological, and dynamical nature from astronomical observations. *Meteoritics and Planetary Science*, *50*(4), 834–849.

Lin, R. P., Meng, C.-I., & Anderson, K. A. (1974). 30- to 100-keV protons upstream from the Earth's bow shock. *Journal of Geophysical Research*, *79*(4), 489–498.

Lue, C., Futaana, Y., Barabash, S., Wieser, M., Holmström, M., Bhardwaj, A., … Wurz, P. (2011). Strong influence of lunar crustal fields on the solar wind flow. *Geophysical Research Letters*, *38*, L03202. https://doi.org/10.1029/2010GL046215

Lui, A. T. Y., Williams, D. J., McEntire, R. W., Christon, S. P., Eastman, T. E., Yamamoto, T., & Kokubun, S. (1998). Ion composition and charge state of energetic particles in flux ropes/plasmoids. *Journal of Geophysical Research*, *103*(A3), 4467–4475.

Matsumoto, T., Tsuchiyama, A., Miyake, A., Noguchi, T., Nakamura, M., Uesugi, K., … Nakano, T. (2015). Surface and internal structures of a space-weathered rim of an Itokawa regolith particle. *Icarus*, *257*, 230–238.

May, P. W., des Pineau Forêts, G., Flower, D. R., Field, D., Allan, N. L., & Purton, J. A. (2000). Sputtering of grains in C-type shocks. *Monthly Notices of the Royal Astronomical Society*, *318*, 809–816.

McFadden, J. P., Kortmann, O., Curtis, D., Dalton, G., Johnson, G., Abiad, R., … Jakosky, B. (2015). MAVEN suprathermal and thermal ion composition (STATIC) instrument. *Space Science Reviews*, *195*, 199–256.

McFadden, J. P., Carlson, C. W., Larson, D., Ludlam, M., Abiad, R., Elliott, B., … Angelopoulos, V. (2008). The THEMIS ESA plasma instrument and in-flight calibration. *Space Science Reviews*, *141*, 277–302.

Murchie, S. L., Britt, D. T., & Pieters, C. M. (2014). The value of Phobos sample return. *Planetary and Space Science*, *102*, 176–182.

Nishino, M. N., Harada, Y., Saito, Y., Tsunakawa, H., Takahashi, F., Yokota, S., … Shimizu, H. (2017). Kaguya observations of the lunar wake in the terrestrial foreshock: Surface potential change by bow-shock reflected ions. *Icarus*, *293*, 45–51.

Noguchi, T., Kimura, M., Hashimoto, T., Konno, M., Nakamura, T., & Zolensky, M. E. (2014). Space weathered rims found on the surfaces of the Itokawa dust particles. *Meteoritics and Planetary Science*, *49*(2), 188–214.

Pieters, C. M., Taylor, L. A., Noble, S. K., Keller, L. P., Hapke, B., Morris, R. V., … Wentworth, S. (2000). Space weathering on airless bodies: Resolving a mystery with lunar samples. *Meteoritics and Planetary Science*, *35*, 1101–1107.

Poppe, A. R., & Curry, S. M. (2014). Martian planetary heavy ion sputtering of Phobos. *Geophysical Research Letters*, *41*, 6335–6341. https://doi.org/10.1002/2014GL061100

Poppe, A. R., Fillingim, M. O., Halekas, J. S., Raeder, J., & Angelopoulos, V. (2016). ARTEMIS observations of terrestrial ionospheric molecular ion outflow at the Moon. *Geophysical Research Letters*, *43*, 6749–6758. https://doi.org/10.1002/2016GL069715

Poppe, A. R., Halekas, J. S., Lue, C., & Fatemi, S. (2017). ARTEMIS observations of the solar wind proton scattering function from lunar crustal magnetic anomalies. *Journal of Geophysical Research: Planets*, *122*, 771–783. https://doi.org/10.1002/2017JE005313

Rahmati, A., Larson, D. E., Cravens, T. E., Lillis, R. J., Dunn, P. A., Halekas, J. S., … Jakosky, B. M. (2015). MAVEN insights into oxygen pickup ions at Mars. *Geophysical Research Letters*, *42*, 8870–8876. https://doi.org/10.1002/2015GL065262

Reames, D. V. (1999). Particle acceleration at the Sun and in the heliosphere. *Space Science Reviews*, *90*, 413–491.

Reames, D. V. (2013). The two sources of solar energetic particles. *Space Science Reviews*, *175*, 53–92.

Reisenfeld, D. B., Wiens, R. C., Barraclough, B. L., Steinberg, J. T., Neugebauer, M., Raines, J., & Zurbuchen, T. H. (2013). Solar wind conditions and composition during the Genesis mission as measured by in situ spacecraft. *Space Science Reviews*, *175*, 125–164.

Schwadron, N. A., Baker, T., Blake, B., Case, A. W., Cooper, J. F., Golightly, M., … Zeitlin, C. (2012). Lunar radiation environment and space weathering from the cosmic ray telescope for the effects of radiation. *Journal of Geophysical Research*, *117*, E00H13. https://doi.org/10.1029/2011JE003978

Seki, K., Hirahara, M., Terasawa, T., Mukai, T., Saito, Y., Machida, S., … Kokubun, S. (1998). Statistical properties and possible supply mechanisms of tailward cold O^+ beams in the lobe/mantle regions. *Journal of Geophysical Research*, *103*, 4477–4493.

Sibeck, D. G., Angelopoulos, V., Brain, D. A., Delory, G. T., Eastwood, J. P., Farrell, W. M., … Weygand, J. M. (2011). ARTEMIS science objectives. In *The ARTEMIS mission* (pp. 27–59). New York: Springer.

Ziegler, J. F., Biersack, J. P., & Littmark, U. (1985). *The stopping and range of ions in solids*. New York: Pergamon Press.

Ziegler, J. F., Biersack, J. P., & Ziegler, M. D. (2008). *SRIM—The stopping and range of ions in matter*. Morrisville, NC: Lulu Press.

Ziegler, J. F., Ziegler, M. D., & Biersack, J. P. (2010). SRIM—The stopping and range of ions in matter (2010). *Nuclear Instruments and Methods in Physics Research Section B*, *268*, 1818–1823.